


© 2021 Optical Society of America. Users may use, reuse, and build upon the article, or use the article for text or data mining, so long as such uses are for non-commercial purposes and appropriate attribution is maintained. All other rights are reserved.

LINK TO ONLINE ABSTRACT IN THE
OSA JOURNAL:

<https://www.osapublishing.org/boe/fulltext.cfm?uri=boe-12-4-1905&id=449003>



Accuracy of homogeneous models for photon diffusion in estimating neonatal cerebral hemodynamics by TD-NIRS

CATERINA AMENDOLA,^{1,5} LORENZO SPINELLI,² DAVIDE CONTINI,¹  AGNESE DE CARLI,³ CESARE MARTINELLI,⁴ MONICA FUMAGALLI,^{3,4} AND ALESSANDRO TORRICELLI^{1,2,6}

¹Dipartimento di Fisica, Politecnico di Milano, Milan, Italy

²Istituto di Fotonica e Nanotecnologie, Consiglio Nazionale delle Ricerche, Milan, Italy

³Fondazione IRCCS Ca' Granda Ospedale Maggiore Policlinico, NICU, Milan, Italy

⁴University of Milan - Department of Clinical Sciences and Community Health, Milan, Italy

⁵caterina.amendola@polimi.it

⁶alessandro.torricelli@polimi.it

Abstract: We assessed the accuracy of homogeneous (semi-infinite, spherical) photon diffusion models in estimating absolute hemodynamic parameters of the neonatal brain in realistic scenarios (ischemia, hyperoxygenation, and hypoventilation) from 1.5 cm interfiber distance TD NIRS measurements. Time-point-spread-functions in 29- and 44-weeks postmenstrual age head meshes were simulated by the Monte Carlo method, convoluted with a real instrument response function, and then fitted with photon diffusion models. The results show good accuracy in retrieving brain oxygen saturation, and severe underestimation of total cerebral hemoglobin, suggesting the need for more complex models of analysis or of larger interfiber distances to precisely monitor all hemodynamic parameters.

© 2021 Optical Society of America under the terms of the [OSA Open Access Publishing Agreement](#)

1. Introduction

Brain injuries are an important cause of morbidity and mortality in neonates. Cerebrovascular disturbances, such as impaired cerebral hemodynamics and autoregulation (CA), are involved in the pathogenesis of brain injury [1–4]. CA is the ability to maintain constant the cerebral blood flow, despite changes in perfusion pressure [5, 6]; and it may be impaired in many neonatal conditions such as prematurity [7], hypoxic–ischemic encephalopathy [8], intracranial hemorrhage [9], congenital heart disease [10]. Failure of CA leaves brain tissues unprotected against strong variations of blood flow and could increase the risk of brain injury and mortality, making cerebral perfusion and oxygenation monitoring techniques necessary in Neonatal Intensive Care Units. Nowadays, many of the techniques clinically used [11, 12] such as positron emission tomography, contrast enhanced magnetic resonance imaging (MRI), Xenon clearance are bulky, need patient transport and immobility, and some of them are invasive or make use of radioactive tracers. Transcranial Doppler ultrasound is widely used in neonatology to measure cerebral blood flow velocity in target artery, but its results are limited to the macro-vasculature [13], and in particular clinical derangement the macro-vasculature blood flow may not reflect the one in cerebral region [14]. Moreover, it is operator-dependent [15] and it does not allow continuous monitoring cerebral hemodynamic parameters. In this scenario, Near Infrared Spectroscopy (NIRS) appears to be an interesting alternative: it is a non-invasive technique which allows for monitoring brain hemodynamics and CA, at bed side [16,17].

NIRS techniques exploit the low absorption of near infrared light by the main biological tissues' constituents, allowing light to penetrate a few cm inside tissues. Differences in absorption spectra

of tissues' constituents (such as oxygenated (O_2Hb) and deoxygenated (HHb) hemoglobin) permit to evaluate their concentration variations in the probed area.

In continuous wave NIRS [18] (CW-NIRS) light of constant intensity is injected in tissues and by measuring backscattered light amplitudes, at different wavelengths, variations of hemoglobin concentration in the probed tissue are retrieved. It is the most widespread NIRS technique, frequently used in neonatology thanks to its lower level of complexity and its stronger presence in the market. As draw back, it does not allow to directly estimate absolute concentrations of HHb and O_2Hb , when a single interfiber distance is used, but only their variations.

Frequency domain NIRS (FD-NIRS) [19] exploits variations, in amplitude and phase of modulated light, due to the interaction of light with biological tissues, whereas time domain NIRS (TD-NIRS) [20] profits from variations in shape and amplitude of injected light pulses with short (*i.e.* picosecond) duration. FD-NIRS and TD-NIRS are more complex techniques as compared to CW-NIRS, but allow to non-invasively estimate absolute concentrations of O_2Hb and HHb , therefore providing estimates also for total hemoglobin ($tHb = O_2Hb + HHb$) and tissue oxygen saturation ($S_tO_2 = O_2Hb / tHb$). Moreover, both FD-NIRS and TD-NIRS have superior depth sensitivity compared to CW-NIRS [21]. NIRS estimates of the hemodynamic parameters are influenced by probed tissues' structures and geometry. Indeed, many studies have been published on the effects of extra cerebral tissues (ECT) on NIRS measurements in the adult head [22–24].

When NIRS techniques are used for monitoring neonatal brain hemodynamics, a precise estimation of vital parameters such as brain tHb and S_tO_2 is essential. Thus, a study on the influence of superficial tissues and head structure is fundamental. The differences in size and curvature between adults and neonates head geometry suggest that separate studies need to be performed. Concerning neonatal head structure, previous works have been addressed to determine the influence of superficial layers and the accuracy in estimating optical properties when CW-NIRS [25, 26] and FD-NIRS [27] are employed. Regarding the accuracy in estimating cerebral hemodynamic parameters in neonates, the only study that have been published up to now is the one by Barker *et al.* [28] in 2014. They investigated the accuracy of FD-NIRS in estimating brain S_tO_2 and tHb . Few TD-NIRS studies have been conducted to determine the optical and hemodynamic properties of neonatal head [29, 30] and some TD-NIRS clinical studies have been performed to monitor neonatal cerebral hemodynamics [31, 32]. To our knowledge no systematic study on the TD-NIRS accuracy in estimating neonatal brain hemodynamics has been performed. In our opinion, precise estimation of critical parameters as tHb and S_tO_2 is fundamental to adopt TD-NIRS as monitoring technique of neonatal brain health.

Therefore, in this work we assessed the accuracy of homogeneous models for photon diffusion in estimating neonatal cerebral hemodynamics by TD-NIRS. We simulated light propagation inside realistic meshes of 29 and 44 weeks' postmenstrual age (PMA) neonates' head structures, through Monte Carlo (MC) method. Absorption coefficient of brain tissue was varied to model realistic hemodynamic scenarios common in preterm neonates (ischemia, hyperoxygenation and hypoventilation). We mimicked realistic photon distribution of time of flight (DTOF) by convolving the simulated time point spread function (TPSF) with the instrument response function (IRF) of the BabyLux device [31]. Finally, the DTOF were analysed with two homogeneous models for photon diffusion: semi-infinite and spherical.

2. Methods

2.1. Mesh-based MC method

TD-NIRS measurements on neonates' heads were simulated with the MC method. In particular, a mesh-based MC tool (MMCLAB [33]) was used to simulate photon migration inside a realistic atlas of three dimensional (3D) head structure [34]. The head models used in our simulations were selected from an online dataset, containing meshes of preterm and term neonates' heads from 29 to 44 weeks PMA [34]. We simulated photon propagation in the two extreme cases,

29 and 44 weeks PMA, to maximize the influence that head structures, dimensions, and shapes would have on the retrieved optical and hemodynamic properties.

The head structures were divided into three domains (see Fig. 1) with different optical properties (absorption coefficient μ_a , and reduced scattering coefficient μ'_s): ECT (comprehensive of scalp and skull), cerebrospinal fluid (CSF), and brain (composed by white matter, grey matter, cerebellum and brainstem).

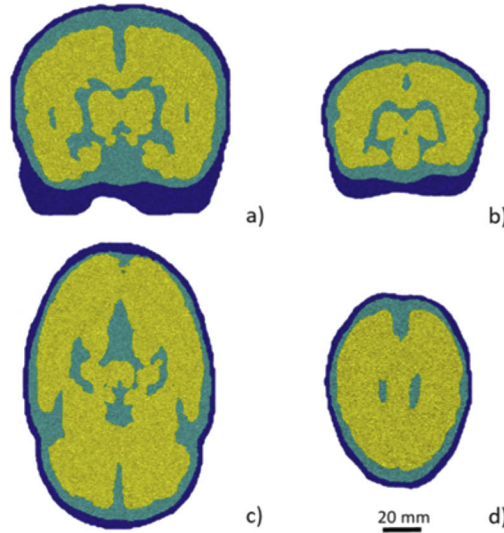


Fig. 1. 2D Image of 44 (a, c) and 29 (b, d) weeks PMA meshes, divided in three domains: ECT (in blue), CSF (green) and brain (yellow). Figure a) and b) show coronal view in the plane identified by Cz (in the 10–20 International EEG system electrode placement), figure c) and d) show axial view in the plane at the middle between injection and detection points.

2.2. Optical and hemodynamic parameters

The optical parameters used as baseline in our simulations were the one selected by Barker *et al.* [28] and are summarized in Table 1. For the ECT, the optical parameters used are the one of the scalp, indeed skull thickness is extremely thin [35], suggesting us to approximate its contribution as negligible. The anisotropy parameter g of head tissues was considered homogeneous and set to 0.89 [36]. The refractive index n was assumed constant over wavelength.

Table 1. Optical parameters assigned to the three tissues types (ECT, CSF, brain) at the two wavelengths of 690 nm and 830 nm [28]. n is the refractive index. Anisotropy coefficient was set to 0.89 for all tissue types.

| Tissues | $\mu_a^{690}(\text{cm}^{-1})$ | $\mu_a^{830}(\text{cm}^{-1})$ | $\mu'_s^{690}(\text{cm}^{-1})$ | $\mu'_s^{830}(\text{cm}^{-1})$ | $n(-)$ |
|---------|-------------------------------|-------------------------------|--------------------------------|--------------------------------|--------|
| ECT | 0.206 | 0.122 | 23.7 | 18.1 | 1.45 |
| CSF | 0.004 | 0.02 | 0.1 | 0.1 | 1.33 |
| Brain | 0.122 | 0.137 | 14.4 | 10.7 | 1.45 |

The absorption coefficient of brain tissue was modified to mimic three hemodynamic scenarios common in preterm neonates: reduction of brain $S_t\text{O}_2$ from 70% to 40% (scenario 1: ischemia); increase of brain $S_t\text{O}_2$ from 70% to 100% (scenario 2: hyperoxygenation); reduction of brain $S_t\text{O}_2$ from 70% to 40% with simultaneous increase of tHb from 53 μM to 93 μM (scenario 3: hypoventilation). The values of O_2Hb , HHb, tHb, $S_t\text{O}_2$ and the correspondent absorption

coefficient (derived by Beer's law [28]) simulated in the brain are reported in Table 2. In deriving the hemodynamic parameters a water fraction of 90% was assumed in the brain [37]. No hemodynamic variations were simulated in ECT and CSF, and their optical properties were maintained constant for each one of the considered scenarios.

Table 2. Brain hemodynamic parameters and correspondent absorption coefficients in the three hemodynamic scenarios: ischemia (scenario 1), hyperoxygenation (scenario 2) and hypoventilation (scenario 3). A constant water fraction of 90% was assumed.

| Scenario | HHb (μM) | O ₂ Hb (μM) | tHb (μM) | S _t O ₂ (%) | μ_a^{690} (cm^{-1}) | μ_a^{830} (cm^{-1}) |
|----------|-----------------------|-------------------------------------|-----------------------|-----------------------------------|------------------------------------|------------------------------------|
| 1 | 16 | 37 | 53 | 70 | 0.122 | 0.137 |
| | 19 | 34 | 53 | 65 | 0.133 | 0.136 |
| | 21 | 32 | 53 | 60 | 0.144 | 0.135 |
| | 24 | 29 | 53 | 55 | 0.156 | 0.134 |
| | 27 | 27 | 53 | 50 | 0.167 | 0.132 |
| | 29 | 24 | 53 | 45 | 0.178 | 0.131 |
| | 32 | 21 | 53 | 40 | 0.189 | 0.130 |
| 2 | 16 | 37 | 53 | 70 | 0.122 | 0.137 |
| | 13 | 40 | 53 | 75 | 0.111 | 0.139 |
| | 11 | 42 | 53 | 80 | 0.098 | 0.140 |
| | 8 | 45 | 53 | 85 | 0.087 | 0.141 |
| | 5 | 48 | 53 | 90 | 0.078 | 0.142 |
| | 3 | 50 | 53 | 95 | 0.066 | 0.144 |
| | 0 | 53 | 53 | 100 | 0.055 | 0.145 |
| 3 | 16 | 37 | 53 | 70 | 0.122 | 0.137 |
| | 20 | 37 | 57 | 65 | 0.143 | 0.144 |
| | 25 | 37 | 62 | 60 | 0.167 | 0.153 |
| | 30 | 37 | 67 | 55 | 0.196 | 0.163 |
| | 37 | 37 | 74 | 50 | 0.231 | 0.175 |
| | 45 | 37 | 82 | 45 | 0.273 | 0.190 |
| | 56 | 37 | 93 | 40 | 0.327 | 0.208 |

The inter-subject variability of tissue optical and hemodynamic properties was reproduced by repeating all simulations considering other eight baseline conditions: i) two different values of μ'_s for ECT ($\pm 25\%$); ii) two different values of μ'_s for brain ($\pm 25\%$); iii) two different values of μ_a for the ECT ($\pm 25\%$); iv) two different values of μ_a for the brain (modeling tHb variations $\pm 25\%$). A scheme of the performed simulations and their use for estimating the error in the optical and hemodynamic parameters is reported in Table 3.

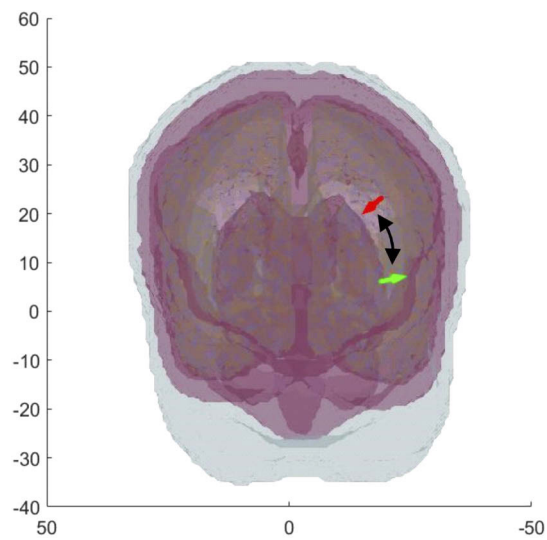
2.3. MC simulations

In each simulation, 10^9 photons were injected in the Afp7 position of 10–20 International system of EEG electrode placement, and the detection point was positioned 15 mm away measured along the scalp surface (Fig. 2). This value was selected to mimic the behavior of BabyLux device [31]: TD-NIRS device designed for monitoring cerebral hemodynamics of preterm neonates.

In our simulations, μ_a values were initially set to 0 cm^{-1} for all tissue types, and the absorption effect was added *a posteriori* [38] by decreasing the photon weight by $\exp(-\mu_{a,i}L_i)$, where $\mu_{a,i}$ and L_i are respectively the absorption coefficient and the pathlength traveled by photons in the *i*-th tissue type. To model a realistic DTOF, the simulated TPSFs were convolved with the IRF of the BabyLux device [31], after IRF normalization to unit area. The IRF (Fig. 3) used were

Table 3. Scheme of the optical and hemodynamic parameters retrieved with the corresponding variations of the baseline, for the three scenarios (Table 2).

| Simulation # | Change with respect to Table 1 | Used for estimating error in μ_a^{brain} , tHb^{brain} , and $S_tO_2^{\text{brain}}$ | Used for estimating error in μ_s^{brain} |
|--------------|--------------------------------|--|---|
| 0 | None | YES | YES |
| 1 | + 25% μ_a^{ECT} | YES | YES |
| 2 | - 25% μ_a^{ECT} | YES | YES |
| 3 | + 25% μ_s^{ECT} | YES | YES |
| 4 | - 25% μ_s^{ECT} | YES | YES |
| 5 | + 25% μ_s^{brain} | YES | NO |
| 6 | - 25% μ_s^{brain} | YES | NO |
| 7 | + 25% μ_a^{brain} | NO | YES |
| 8 | - 25% μ_a^{brain} | NO | YES |

**Fig. 2.** 2D projection of source (red arrow) and detection (green arrow) position along the scalp surface. Detection is positioned in the AFp7 of the 10–20 International system of EEG electrode placement, the source 15 mm away along scalp surface.

characterized by full width at half maximum (FWHM) of 190 ps, and time bin of 25 ps. Shot noise was added, as Poisson distribution [39], while other noise sources (thermal noise and dark current) were considered negligible in the case of hybrid photomultiplier tube, detector type used in BabyLux device [31].

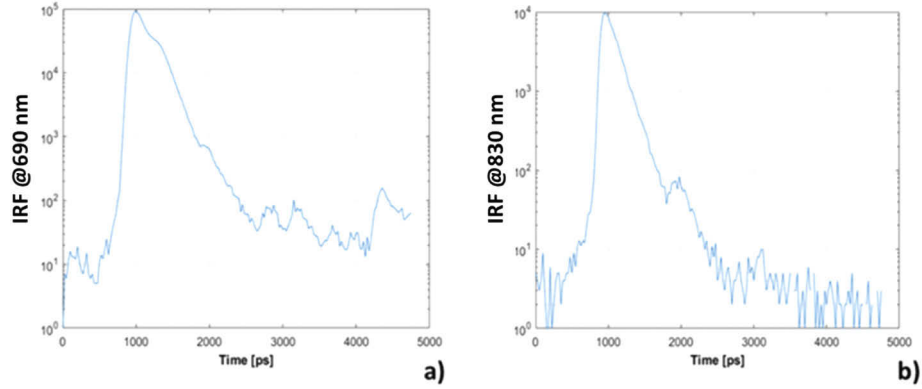


Fig. 3. IRF of the BabyLux device at 690 nm (panel a), and 830 nm (panel b).

The collected photons were approximately 10^5 and $5 \cdot 10^4$ in the case of 29 and 44 weeks PMA mesh, respectively. To reduce statistical noise, all simulations were repeated 10 times, and the results averaged. All simulations were performed at 690 nm and 830 nm.

2.4. DE model for the fitting procedure

Absorption and reduced scattering coefficients were retrieved by fitting the simulated DTOF with the solution of the Diffusion Equation for both a homogeneous semi-infinite model [40] and a homogeneous spherical model [41]. In the latter case, to take into account the effect of the finite volume of the head, we approximated the neonates' head to a sphere, considering the distance between Inion and Nasion positions (I_z and N_z) as the diameter of the sphere: $d = 2r = (I_z - N_z)$. The source detector distance $\rho = 15$ mm was measured along the sphere surface, and the angular distance θ between injected light and photon collection was computed as the angle underlying the circumference arc of length equal to the inter-fiber distance ($\theta = \rho/r$). The partial current boundary condition (PCBC) was applied to solve the DE for both the semi-infinite and the spherical homogeneous model.

The accuracy of hemodynamic parameters estimated with the semi-infinite and spherical homogeneous model for photon migration was evaluated through the mean absolute percent error (MAPE) computed over the 10 repetitions of simulation 0 in Table 3:

$$\langle MAPE_X \rangle_{10 \text{ rep}} = 100 \frac{\langle |X_{estimated} - X_{simulated}| \rangle_{10 \text{ rep}}}{X_{simulated}} \quad (1)$$

where X is the desired hemodynamic parameter. In Sec.3, the mean MAPE for the three studied scenarios (Table 2) is reported, estimated as the average over the 70 simulations done for each of these conditions (the 10 repetitions of all the 7 conditions, reported in Table 2, for each scenario of simulation 0 of Table 3). Variations of optical parameters (simulations from 1 to 6 in Table 3) generate a dispersion (D_X) of estimated $MAPE_X$, which was computed as:

$$\langle D_X \rangle_{10 \text{ rep}} = 100 \frac{\max_n \langle |X_{sim \#n} - X_{sim 0}| \rangle_{10 \text{ rep}}}{\langle X_{sim 0} \rangle_{10 \text{ rep}}} \quad (2)$$

Where, $X_{sim\ 0}$ is the hemodynamic parameters retrieved for simulation 0 reported in Table 3, and $X_{sim\ \#n}$ is the hemodynamic parameters retrieved for simulation #n reported in Table 3, varying n from 1 to 6.

3. Results

3.1. Semi-infinite homogeneous model analysis

3.1.1. Optical parameters

The reduced scattering coefficients retrieved by analyzing simulated DTOF with the semi-infinite homogeneous model at 690 nm and 830 nm are reported in Fig. 4, for the three scenarios described in Table 2. The corresponding absorption coefficients can be founded in the Supplement 1 (Sec. S2.1.1). In all cases the estimated reduced scattering coefficient shows an underestimation with respect to the nominal values (Fig. 4), and that is more evident in case of 29 weeks PMA mesh. The effect of inter subject variability (variations of $\pm 25\%$ of μ_a^{ECT} , μ_a^{brain} and μ_s^{ECT}) is reported as shadows determined by the maximum and minimum values of the estimated parameter. The parameter which mostly influences the range of variation of μ_s was μ_s^{ECT} . Variations of $\pm 25\%$ of all the other optical properties (μ_a^{ECT} , μ_a^{brain}) weakly affect the retrieved μ_s .

3.1.2. Hemodynamic parameters

Hemodynamic parameters tHb and S_tO_2 for the three analyzed conditions in Table 2 are presented in Fig. 5. HHb, O_2Hb , and the corresponding absorption coefficients, can be founded in Supplement 1 (Sec. S2.1.1 and Sec. S2.1.2). The shadows represent the range of variations due to intersubject variability of optical properties ($\pm 25\%$ of μ_a^{ECT} , μ_s^{brain} , and μ_s^{ECT}). tHb estimated with the semi-infinite homogeneous model is lower than the nominal values in the brain. Comparing the results obtained for the two meshes, it is evident that tHb retrieved for 29 weeks PMA mesh is underestimated with respect to 44 weeks PMA mesh. Indeed, $MAPE_{tHb}$ is higher and it reaches its maximum value when scenario 3 was simulated (Table 4). Conversely, S_tO_2 estimates are close to the values simulated in the brain, and the $MAPE_{S_tO_2}$ is much lower than $MAPE_{tHb}$ (Table 4). Also, the range of variations due to intersubject variability is reduced compared to tHb, as the reduction of dimensions of blue and red shadows in Fig. 5 suggests.

Table 4. MAPE of simulation 0 (Table 3) and error dispersion (D) due to optical parameter variations (simulations from 1 to 6 in Table 3) for the hemodynamic parameter tHb and S_tO_2 estimated with the semi-infinite homogeneous model, averaged over all the simulations of each scenario (Table 2).

| Scenario | Variable | 29 weeks | | 44 weeks | |
|----------|----------|-----------|--------|-----------|--------|
| | | Mean MAPE | Mean D | Mean MAPE | Mean D |
| 1 | tHb | 22.8 | 6.6 | 14.4 | 7.5 |
| | S_tO_2 | 3.5 | 4.3 | 8.4 | 7.1 |
| 2 | tHb | 23.3 | 5.3 | 15.1 | 7.7 |
| | S_tO_2 | 7.0 | 1.2 | 9.15 | 2.8 |
| 3 | tHb | 27.3 | 5.6 | 19.85 | 3.6 |
| | S_tO_2 | 7.1 | 3.9 | 10.0 | 4.5 |

3.2. Spherical homogeneous model analysis

To reduce the error related to surface curvatures, and consider the finite volume of the neonates' heads, the simulated data were analyzed with a spherical homogeneous model for photon migration. The radius of the spheres was computed as half of the distance between Inion and Nasion and resulted to be 41 mm and 59 mm for 29 and 44 weeks meshes, respectively.

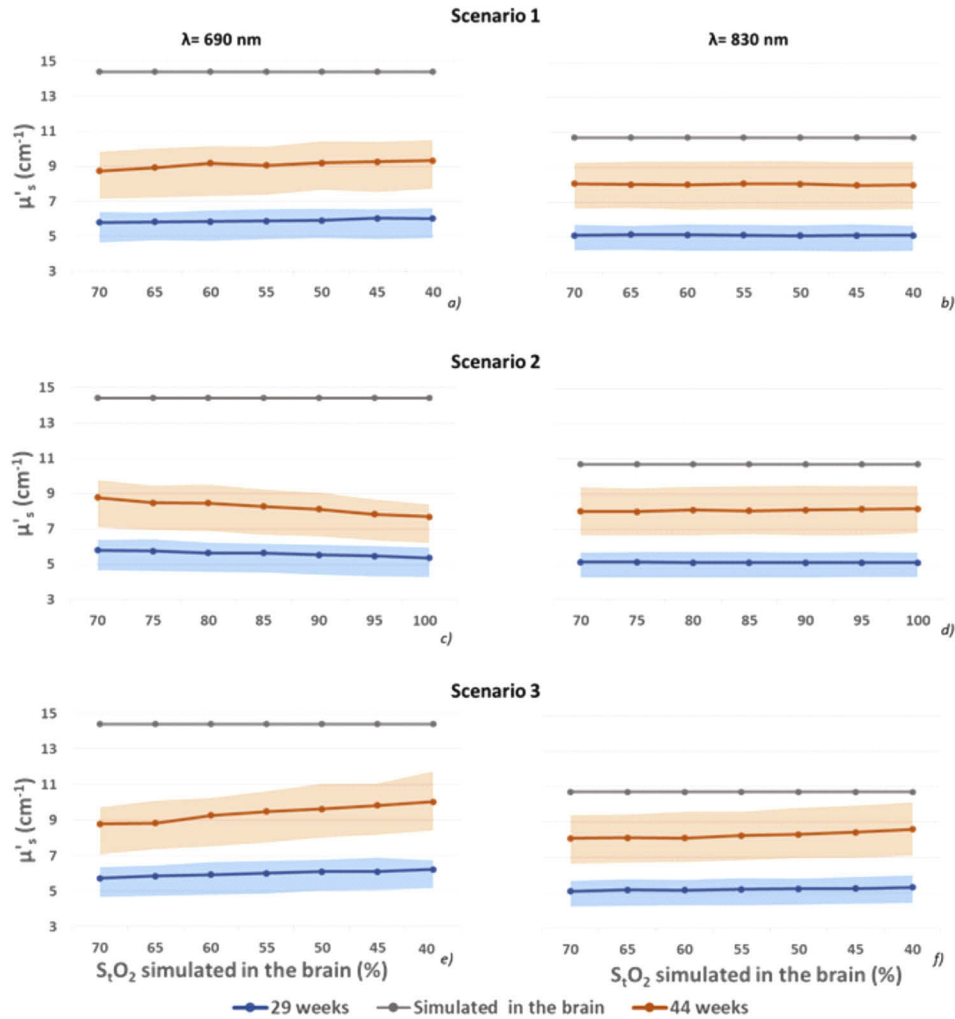


Fig. 4. Reduced scattering coefficient estimated for 29 (blue curve) and 44 (red curve) weeks PMA meshes with the semi-infinite homogeneous model. The gray curve represents the nominal values. The shadows represent the range of reduced scattering variations (maximum and minimum values) due to inter-subject variability. Left column and right column represent the values estimated at 690 nm and 830 nm, respectively. Top row represents the scenario 1, middle row scenario 2, and bottom row scenario 3 in Table 2.

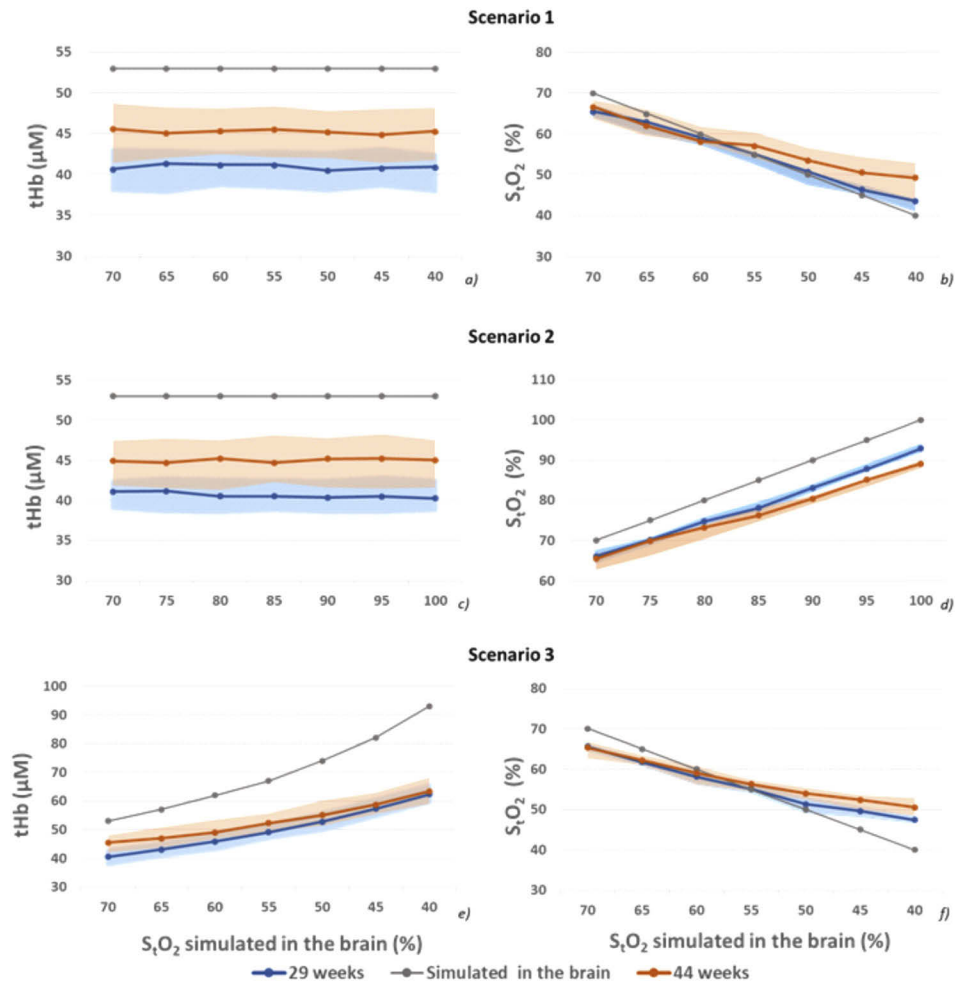


Fig. 5. tHb (left column) and S_tO_2 (right column) estimated for 29 (blue curve) and 44 (red curve) weeks PMA meshes with the semi-infinite homogeneous mode for scenario 1 (top row), scenario 2 (middle row), and scenario 3 (bottom row) of Table 2. The gray curve in each panel represents the nominal values. The shadows represent the range of variations (maximum and minimum values reached) due to inter-subject variability of optical parameters.

3.2.1. Optical parameters

The estimated reduced scattering coefficient, at 690 nm and 830 nm, are shown in Fig. 6. The values reported are the one estimated for simulation 0 in Table 3, and the shadows represent the range of variability due to intersubject variability ($\pm 25\% \mu_s^{\text{ECT}}$, $\pm 25\% \mu_a^{\text{ECT}}$, $\pm 25\% \text{tHb}^{\text{brain}}$). The results are like those discussed in 3.1.1. Also, in this case the estimated scattering coefficients is lower than the nominal one in the brain, and in case of 29 weeks PMA mesh the underestimation is stronger. Moreover, as described in paragraph 3.1.1, μ_s^{ECT} is the parameter which mostly influences the estimates. Comparing the results shown in Fig. 6 and Fig. 4, the scattering coefficient retrieved with the spherical homogeneous model are higher than the one estimated with the semi-infinite homogeneous model, therefore closer to the nominal values.

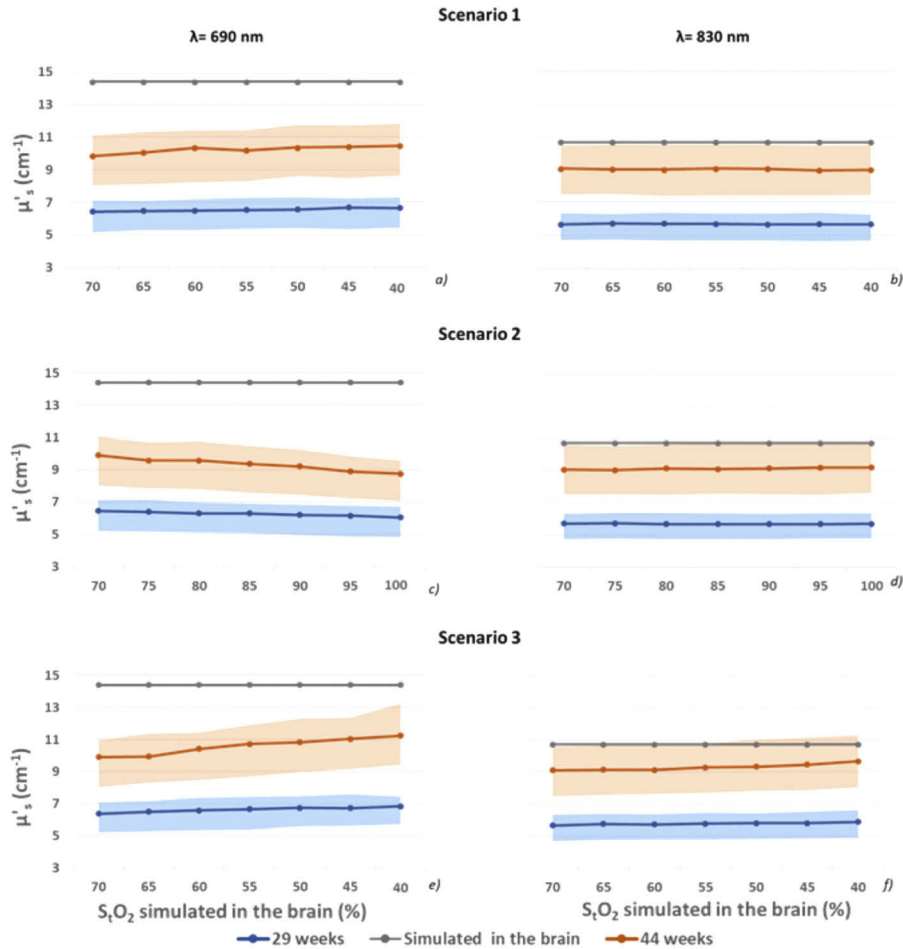


Fig. 6. Reduced scattering coefficient estimated for 29 (blue curve) and 44 (red curve) weeks PMA meshes with the spherical homogeneous model. The gray curve represents the nominal values. The shadows represent the range of reduced scattering variations (maximum and minimum values) due to inter-subject variability. Left column and right column represent the values estimated at 690 nm and 830 nm, respectively. Top row represents the scenario 1, middle row scenario 2, and bottom row scenario 3 of Table 2.

3.2.2. Hemodynamic parameters

Hemodynamic parameters estimated with the spherical model for photon migration for the three scenarios of Table 2 are summarized in Fig. 7. Also in this case the reported values are the one estimated for simulation 0 of Table 3, and the shadows represent the range of variations due to intersubject variability ($\pm 25\% \mu_s^{\text{ECT}}$, $\pm 25\% \mu_s^{\text{brain}}$, $\pm 25\% \mu_a^{\text{ECT}}$). Obtained results are like those reported in 3.1.2 for the semi-infinite homogeneous model. tHb is underestimated, and it appears more evident in case of 29 weeks PMA mesh. The tHb retrieved with spherical model shows lower values than the one obtained with the semi-infinite homogeneous model analysis (Fig. 5 and Fig. 7), and the corresponding MAPE_{tHb} are higher (Table 5).

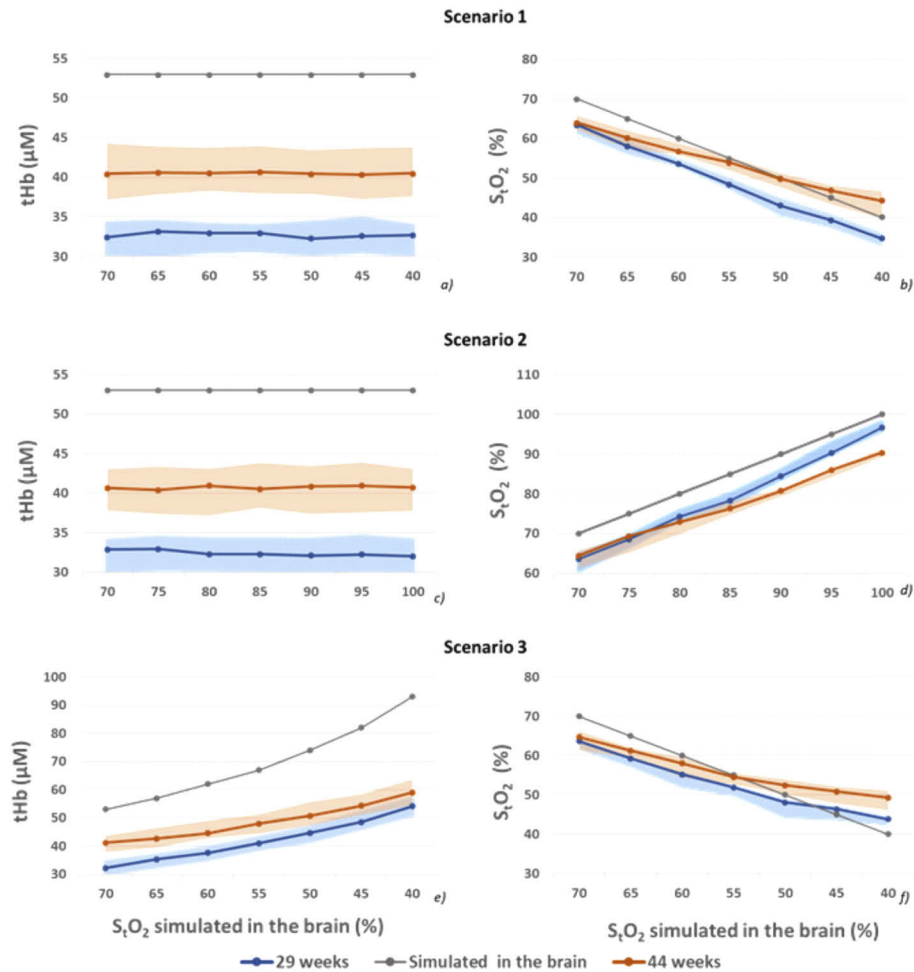


Fig. 7. tHb (left column) and S_tO_2 (right column) estimated for 29 (blue curve) and 44 (red curve) weeks PMA meshes with the spherical homogeneous mode for scenario 1 (top row), scenario 2 (middle row), and scenario 3 (bottom row). The gray curve in each panel represents the nominal values. The shadows represent the range of variations (maximum and minimum values reached) due to inter-subject variability of optical parameters.

Conversely, as in 3.1.2 the estimated S_tO_2 shows values like the nominal ones in the brain. Slopes of the curves reproducing estimated S_tO_2 values (red and blue curves in Fig. 7 b, d, f) are higher than in semi-infinite homogeneous model, and more similar to the nominal S_tO_2 values in the brain (grey curves in Fig. 7 b, d, f).

Table 5. MAPE of simulation 0 (Table 3) and error dispersion (D) due to optical parameter variations (simulations from 1 to 6 in Table 3) for the hemodynamic parameter tHb and S_tO₂ estimated with the spherical homogeneous model, averaged over all the simulations of each scenario (Table 2).

| Scenario | Variable | 29 weeks | | 44 weeks | |
|----------|-------------------------------|-----------|--------|-----------|--------|
| | | Mean MAPE | Mean D | Mean MAPE | Mean D |
| 1 | tHb | 38.2 | 7.0 | 22.6 | 8.15 |
| | S _t O ₂ | 10.0 | 6.1 | 6.5 | 7.5 |
| 2 | tHb | 38.9 | 6.9 | 23.2 | 8.0 |
| | S _t O ₂ | 6.8 | 2.4 | 9.2 | 3.2 |
| 3 | tHb | 39.6 | 6.0 | 25.5 | 8.5 |
| | S _t O ₂ | 6.8 | 5.2 | 8.9 | 5.3 |

4. Discussions

In this work we aimed to assess the accuracy of homogeneous models for TD-NIRS in measuring brain optical properties and hemodynamic parameters in neonates. Mesh-based MC tool was used to simulate photon propagation inside realistic atlases of head structures. Neonates' fast growth, and consequent change of head structure, was considered by analyzing TD-NIRS signals in two meshes relative to 29 and 44 weeks PMA neonates' head. The interfiber distance was set to 15 mm to mimic the behavior of the BabyLux device. The choice of the 15 mm interfiber distance was a tradeoff between average penetration depth through neonate head tissues and bulkiness of the probe. The thickness of superficial tissues in the region (5 mm of radius around injection and detection position) of our simulations were: for ECT 2.7 mm and 3.5 mm, for CSF 2.5 mm and 3.9 mm, in 29 and 44 weeks PMA meshes, respectively. The thin layer of ECT and the small absorption and scattering coefficients of CSF allow detected light to penetrate in the deep tissue of the brain. Indeed, the percentages of pathlength travelled by photon in the three domains (for simulation 0 of Table 3) are: ECT 48% (55%), CSF 17% (11%), brain 35% (34%) for 29 (44) weeks PMA mesh. Simulations results were then analyzed with two analytical models for photon migration: semi-infinite homogeneous model, which is one of the most widespread models of analysis because of its low level of complexity; and spherical homogeneous model, considered to reduce the effects of head curvature and finite volume. The radii of the spheres used to represent neonates' head were chosen, as reported in Sec. 2.3, as a half of the distance between Inion and Nasion position, allowing to adapt this model of analysis also in case of real life measurements. In this section the results obtained, presented in Sec. 3, will be discussed.

4.1. Reduced scattering coefficients

4.1.1. Effects of superficial layers

The reduced scattering coefficient shows a systematic underestimation with both the semi-infinite (Fig. 4) and the spherical (Fig. 6) homogeneous model. The error is higher in case of spherical homogeneous model and 29 weeks PMA mesh. It is well known as reported by Comelli *et al.* [42], that, when a homogeneous model is used, the reduced scattering coefficient is strongly influenced by superficial layers. The presence of CSF, which is a low scattering media, could affect the retrieved μ'_s , in both models, and it is probably the cause of the μ'_s underestimation. Ancora *et al.* [24] observed no peak shift on simulated DTOF when CSF thickness was increased, which suggests that an increase of CSF does not influence the retrieved scattering coefficient. However, they simulated an adult head structure, with mean ECT thickness of 12.5 mm. Early photons, which are the ones that mostly affect peak shift, have very low probability to travel inside CSF layer. In case of our work, instead, photon propagation was simulated on newborns' head structures, which are characterized by a lower ECT thickness (about 3 mm of thickness),

making the probability of early photons to travel inside CSF layer not negligible, and with the consequent result of affecting the retrieved scattering coefficient.

Head dimensions and its structure strongly affect sensitivity of TD-NIRS in retrieving brain optical properties. Indeed, the differences obtained in the estimated scattering coefficients of the two meshes for both model of analysis (see Fig. 4 and Fig. 6) could be related to the different thickness of ECT layer in 29 and 44 weeks PMA head structures. ECT is thicker in 44 weeks PMA mesh, with respect to 29 weeks PMA mesh (3.5 mm and 2.7 mm in case of 44–29 weeks PMA mesh, respectively), leading to a stronger influence of that tissue in the estimation of reduced scattering coefficient. This could be the cause for the higher value of μ'_s retrieved in case of 44 week PMA mesh. Indeed, being $\mu'_s{}^{\text{ECT}}$ higher than $\mu'_s{}^{\text{CSF}}$ and $\mu'_s{}^{\text{brain}}$, an increment of ECT thickness could explain the enhancement in the estimation of reduced scattering coefficient for 44 weeks PMA mesh. Thus, the smaller underestimation of scattering coefficients in the 44 weeks PMA head structures is likely due to a combination of the two effects discussed in the previous rows related to the presence of both ECT and CSF: the presence of the CSF in very shallow layer causes a strong reduction in the estimated μ'_s ; on the other side the presence of the ECT causes an increase of the estimated μ'_s and compensates the CSF effects. The higher the ECT thickness, the stronger is its influence, and its compensation of the CSF effect. Indeed, the percentage pathlength travelled by detected photons in the CSF is higher in 29 weeks PMA mesh (17%) than in 44 weeks PMA mesh (11%), while the percentage pathlength travelled in the ECT presents an opposite behaviour: it is higher in 44 weeks PMA mesh (55%), and lower (48%) in 29 weeks PMA mesh. Therefore, in 44 weeks PMA mesh the estimation error is lower, even if the superficial layer thickness is higher.

Moreover, as reported in Secs. 3.1.1 and 3.2.1, the parameter which mostly influences the range of variation (red and blue shadows in Fig. 4 and Fig. 6) of estimated μ'_s is $\mu'_s{}^{\text{ECT}}$. Combining the two discussed effects, that is higher thickness of ECT for 44 weeks PMA mesh, and the strong influence of $\mu'_s{}^{\text{ECT}}$ variations on retrieved scattering coefficient, we can justify the larger dimension of the shadows in case of 44 (red shadows in Fig. 4 and Fig. 6) with respect to the case of 29 weeks PMA mesh (blue shadows in Fig. 4 and Fig. 6).

4.1.2. Effects of head curvature

Comparing the results obtained with semi-infinite and spherical homogeneous model for photon migration, the estimated values of reduced scattering coefficient are smaller when semi-infinite homogeneous model is applied (see Fig. 4 and Fig. 6). This result is in accordance with previous findings: Sassaroli *et al.* [41] investigated the accuracy of semi-infinite, cylindrical and spherical homogeneous models of analysis in retrieving optical properties of MC simulations on spherical geometry. They observed an underestimation of scattering coefficient, which increases with source-detector distance, when the semi-infinite homogeneous model was applied. They also observed small errors when wrong radius of curvature was used in the analysis, which empower the solidity of our approximation in measuring sphere radius. This result highlights the influence of head curvature on retrieved optical properties, and the importance of considering an appropriate model to take into account head curvature.

4.2. Hemodynamic parameters

4.2.1. Effects of superficial layers

As in case of reduced scattering coefficient, also total hemoglobin concentration was strongly underestimated (see Fig. 5 and Fig. 7). In general, optical properties are affected by the presence of superficial layers [42], and variations of absorption coefficients due to ECT and CSF layer are reflected in retrieved hemodynamic parameters. Also in this case, the presence of CSF layer affects hemoglobin concentration, and could be the cause of its underestimation. As reported from Ancora *et al.* [24], by analyzing the behavior of late-photons, a CSF layer thickness

increase causes DTOF curves to exhibit less steep slopes, suggesting a reduction in the absorption coefficients retrieved from DTOF curves. Reduction of the absorption coefficient causes tHb underestimation, which is in accordance with previous findings. For instance, Barker *et al.* [28] simulated multidistance FD-NIRS measurements on neonate's head structure, considering different source detector distances (10–25 mm, 15–30 mm, 20–35 mm, and 25–40 mm), and obtained lower concentration of tHb compared to that simulated in the brain. Discrepancies with respect to brain tHb were lower when source detector distance was increased, confirming that the possible cause could be the influence of superficial layers.

As in case of reduced scattering coefficient, results for 44 weeks PMA mesh show lower MAPE_{tHb} , due to the thicker ECT layer and a less important effect of the CSF layer.

It is worth noting that $S_t\text{O}_2$ is weakly influenced by ECT and CSF layers, probably O_2Hb and HHb underestimation compensate in some way when saturation is computed, and a better sensitivity to brain saturation is obtained (with $\text{MAPE}_{S_t\text{O}_2}$ much lower than in case of tHb, see Table 4 and Table 5).

4.2.2. Effects of head curvature

Comparing the results presented in Fig. 5 and Fig. 7, it appears evident that values retrieved for tHb are lower when spherical homogeneous model is used to analyze simulated DTOF. This result is a consequence of the lower absorption coefficient obtained with spherical homogeneous model, than with semi-infinite homogeneous model, and it agrees with literature. Indeed, Sassaroli *et al.* [41] observed an overestimation of absorption coefficient when semi-infinite homogeneous model was used to analyze simulations on spherical (and cylindrical) geometries.

Concerning $S_t\text{O}_2$, the main difference among the two models is the slope of the curves representing the estimated $S_t\text{O}_2$ (Table 6), which is higher in case of spherical homogeneous model. It appears more evident in case of Ischemia (Fig. 5(b) and Fig. 7(b)), where the angular coefficient of the linear regression curve fitting the retrieved $S_t\text{O}_2$ rises from 0.77, for semi-infinite homogeneous model, to 0.98 for spherical homogeneous model: this fact allows to better retrieve $S_t\text{O}_2$ variations. On the contrary, a slight increase of $\text{MAPE}_{S_t\text{O}_2}$ can be observed in case of spherical homogeneous model.

Table 6. Angular coefficient of the linear regression curve that best fit $S_t\text{O}_2$ estimated from simulation 0 (Table 3) with the semi-infinite and spherical homogeneous model, averaged over 10 repeated simulations of each scenario (Table 2).

| Scenario | 29 weeks PMA mesh | | 44 weeks PMA mesh | |
|----------|---------------------|-----------------|---------------------|-----------------|
| | semi-infinite model | spherical model | semi-infinite model | spherical model |
| 1 | 0.77 | 0.98 | 0.60 | 0.67 |
| 2 | 0.90 | 1.11 | 0.80 | 0.87 |
| 3 | 0.61 | 0.67 | 0.52 | 0.55 |

Differences between the two models of analysis are stronger when simulations on 29 weeks PMA mesh are considered, probably as consequence of the smaller radius of the sphere (41 mm) used to model head structure, compared to the one used in case of 44 weeks PMA mesh (59 mm). Indeed, the higher is the radius, the better is the semi-infinite approximation as model of analysis.

4.2.3. Effects of the increase of tHb

As presented in Table 2, $S_t\text{O}_2$ values simulated in the brain for scenario 1 and 3 were the same (from 70% to 40%), however tHb is constant in case of scenario 1, and increases in case of scenario 3. As a consequence, brain absorption coefficients at the two wavelengths were higher in case of scenario 3 (Table 2). As suggested by Fig. 5(b) and (f) (and in case of spherical homogeneous model Fig. 7(b) and (f)), an increase of absorption coefficient of the brain affects

not only the estimation of tHb, but also the retrieved S_tO_2 . The slope of the S_tO_2 curves retrieved for scenario 3, in Fig. 5(f) (and Fig. 7(f)), is smaller than that one in Fig. 5(b) (and Fig. 7(b)) for scenario 1, suggesting that an increase of brain tHb (and absorption coefficient) reduces the sensitivity of TD-NIRS in measuring brain saturation.

Moreover, the tHb increase leads to shadows enlargement. In our opinion, it could be related to an increase of the absorption coefficient of the deeper tissue (*i.e.* brain), which causes a reduction of detected photons that travelled for longer time inside the brain. Thus, the sensitivity to superficial layers (ECT and CSF) increases, together with the dispersion of retrieved tHb values: as a matter of fact, the parameter which mostly influences the dimension of shadow areas is μ_a^{ECT} .

5. Conclusions

In this work we studied the sensitivity of TD-NIRS in assessing neonatal brain hemodynamic parameters, when homogenous models of analysis are employed. We considered differences in head morphology between preterm and term neonates, simulating light propagation in realistic 3D head structures of 29 and 44 weeks PMA newborns, using MC method. Real life measurements were modelled, varying brain absorption coefficients according to three common conditions in neonates: ischemia (scenario 1), hyperoxygenation (scenario 2) and hypoventilation (scenario 3). Simulated DTOF were analyzed with two analytical homogeneous models for photon migration based on Diffusion Equation: semi-infinite and spherical. Effects of superficial layers and head curvature on retrieved optical and hemodynamic parameters were analyzed, highlighting differences between the two meshes and the two models adopted for analysis. The results presented in Sec. 3 indicate an underestimation of brain total hemoglobin concentration, probably related to the influence of superficial layers, which was more evident in the case of 29 weeks PMA mesh and spherical homogeneous model. Indeed, the CSF strongly influenced the retrieved optical and hemodynamic parameters, and due to its low scattering and absorption coefficients (two order of magnitude lower than ECT and brain), it causes a reduction of estimated brain parameters. On the contrary the ECT is characterized by higher optical properties than CSF and brain, and its presence causes an increase of the retrieved brain optical properties. Thus, the effect of ECT partially balances the one of CSF: the higher the thickness of ECT, the stronger is the balance, and the lower is the underestimation. Conversely, the estimated S_tO_2 exhibits good accuracy to brain values, and low values of $MAPE_{S_tO_2}$. These results were in accordance with a previous work [28], where sensitivity of multi-distance FD-NIRS on neonates hemodynamic shows similar behavior.

Head curvature influenced hemodynamic parameters: as consequence, we observed that spherical homogeneous model of analysis allows to better retrieve brain saturation variations.

The presented results empower the ability of TD-NIRS technique in monitoring neonatal brain hemodynamics but highlight the need for more complex methods of analysis which allow to reduce the influence of superficial layers and head curvatures: a possibility could be the use of MC or other numerical fitting procedures that exploits generalized atlases of three dimensional head structures, or the use of layered model of analysis.

Funding. H2020 Future and Emerging Technologies (863087).

Acknowledgments. This research was partially funded by the Horizon 2020 Framework Programme of the European Union under grant agreement number 863087.

Disclosures. The authors declare that there are no conflicts of interest related to this article.

Data availability. Data underlying the results presented in this paper are not publicly available at this time but may be obtained from the authors upon reasonable request.

Supplemental document. See [Supplement 1](#) for supporting content.

References

1. J. M. Perlman, J. B. Mcmenamin, and J. J. Volpe, "Fluctuating cerebral blood-flow velocity in respiratory-distress syndrome: relation to the development of intraventricular hemorrhage," *N. Engl. J. Med.* **309**(4), 204–209 (1983).
2. E. Hatzidaki, E. Giahnakis, S. Maraka, E. Korakaki, A. Manoura, E. Saitakis, I. Papamastoraki, K. M. Margari, and C. Giannakopoulou, "Risk factors for periventricular leukomalacia," *Acta Obstet. Gynecol. Scand.* **88**(1), 110–115 (2009).
3. V. M. Miall-Allen, L. S. De Vries, and A. G. L. Whitelaw, "Mean arterial blood pressure and neonatal cerebral lesions," *Arch. Dis. Child.* **62**(10), 1068–1069 (1987).
4. H. C. Lou, "Perinatal hypoxic-ischemic brain damage and intraventricular hemorrhage: a pathogenetic model," *Arch. Neurol.* **37**(9), 585–587 (1980).
5. C. J. Rhee, C. S. da Costa, T. Austin, K. M. Brady, M. Czosnyka, and J. K. Lee, "Neonatal cerebrovascular autoregulation," *Pediatr. Res.* **84**(5), 602–610 (2018).
6. G. Greisen, "Autoregulation of cerebral blood flow in newborn babies," *Early Hum. Dev.* **81**(5), 423–428 (2005).
7. J. S. Soul, P. E. Hammer, M. Tsuji, J. P. Saul, H. Bassan, C. Limperopoulos, D. N. Disalvo, M. Moore, P. Akins, S. Ringer, J. J. Volpe, F. Trachtenberg, and A. J. Du Plessis, "Fluctuating pressure-passivity is common in the cerebral circulation of sick premature infants," *Pediatr. Res.* **61**(4), 467–473 (2007).
8. H. C. Lou, N. A. Lassen, and B. Friis-Hansen, "Impaired autoregulation of cerebral blood flow in the distressed newborn infant," *J. Pediatr.* **94**(1), 118–121 (1979).
9. D. A. Godoy, A. Seifi, D. Garza, S. Lubillo-Montenegro, and F. Murillo-Cabezas, "Hyperventilation therapy for control of posttraumatic intracranial hypertension," *Front. Neurol.* **8**, 250 (2017).
10. A. N. Massaro, R. B. Govindan, G. Vezina, T. Chang, N. N. Andescavage, Y. Wang, T. Al-Shargabi, M. Metzler, K. Harris, and A. J. du Plessis, "Impaired cerebral autoregulation and brain injury in newborns with hypoxic-ischemic encephalopathy treated with hypothermia," *J. Neurophysiol.* **114**(2), 818–824 (2015).
11. S. P. Klein, B. Depreitere, and G. Meyfroidt, "How i monitor cerebral autoregulation," *Crit Care* **23**(1), 160 (2019).
12. K. D. Liem and G. Greisen, "Monitoring of cerebral haemodynamics in newborn infants," *Early Hum. Dev.* **86**(3), 155–158 (2010).
13. P. Zirak, R. Delgado-Mederos, J. Martí-Fàbregas, and T. Durduran, "Effects of acetazolamide on the micro- and macro-vascular cerebral hemodynamics: a diffuse optical and transcranial doppler ultrasound study," *Biomed. Opt. Express* **1**(5), 1443–1459 (2010).
14. M. Thoresen, K. Haaland, and P. A. Steen, "Cerebral Doppler and misrepresentation of flow changes," *Arch. Dis. Child.* **71**(2), F103–F106 (1994).
15. M. Wintermark, M. Sesay, E. Barbier, K. Borbély, W. P. Dillon, J. D. Eastwood, T. C. Glenn, C. B. Grandin, S. Pedraza, J.-F. Soustiel, T. Nariai, G. Zaharchuk, J.-M. Caillé, V. Dousset, and H. Yonas, "Comparative overview of brain perfusion imaging techniques," *Stroke* **36**(9), e83–e99 (2005).
16. F. Lange and I. Tachtsidis, "Clinical brain monitoring with time domain NIRS: A review and future perspectives," *Appl. Sci.* **9**(8), 1612 (2019).
17. L. M. L. Dix, F. van Bel, and P. M. A. Lemmers, "Monitoring cerebral oxygenation in neonates: An update," *Front. Pediatr.* **5**, 46 (2017).
18. F. Scholkmann, S. Kleiser, A. J. Metz, R. Zimmermann, J. Mata Pavia, U. Wolf, and M. Wolf, "A review on continuous wave functional near-infrared spectroscopy and imaging instrumentation and methodology," *NeuroImage* **85**, 6–27 (2014).
19. S. Fantini and A. Sassaroli, "Frequency-domain techniques for cerebral and functional near-infrared spectroscopy," *Front. Neurosci.* **14**, 300 (2020).
20. A. Torricelli, D. Contini, A. Pifferi, M. Caffini, R. Re, L. Zucchelli, and L. Spinelli, "Time domain functional NIRS imaging for human brain mapping," *NeuroImage* **85**, 28–50 (2014).
21. S. Gunadi, T. S. Leung, C. E. Elwell, and I. Tachtsidis, "Spatial sensitivity and penetration depth of three cerebral oxygenation monitors," *Biomed. Opt. Express* **5**(9), 2896–2912 (2014).
22. G. E. Strangman, Q. Zhang, and Z. Li, "Scalp and skull influence on near infrared photon propagation in the Colin27 brain template," *NeuroImage* **85**, 136–149 (2014).
23. J. Selb, D. A. Boas, S.-T. Chan, K. C. Evans, E. M. Buckley, and S. A. Carp, "Sensitivity of near-infrared spectroscopy and diffuse correlation spectroscopy to brain hemodynamics: simulations and experimental findings during hypercapnia," *Neurophotonics* **1**(1), 015005 (2014).
24. D. Ancora, L. Qiu, G. Zacharakis, L. Spinelli, A. Torricelli, and A. Pifferi, "Noninvasive optical estimation of CSF thickness for brain-atrophy monitoring," *Biomed. Opt. Express* **9**(9), 4094–4112 (2018).
25. Y. Fukui, Y. Ajichi, and E. Okada, "Monte Carlo prediction of near-infrared light propagation in realistic adult and neonatal head models," *Appl. Opt.* **42**(16), 2881–2887 (2003).
26. M. Wolf, M. Keel, V. Dietz, K. Von Siebenthal, H. U. Bucher, and O. Baenziger, "The influence of a clear layer on near-infrared spectrophotometry measurements using a liquid neonatal head phantom," *Phys. Med. Biol.* **44**(7), 1743–1753 (1999).
27. M. Dehaes, P. E. Grant, D. D. Sliva, N. Roche-Labarbe, R. Pienaar, D. A. Boas, M. A. Franceschini, and J. Selb, "Assessment of the frequency-domain multi-distance method to evaluate the brain optical properties: Monte Carlo simulations from neonate to adult," *Biomed. Opt. Express* **2**(3), 552–562 (2011).

28. J. W. Barker, A. Panigrahy, and T. J. Huppert, "Accuracy of oxygen saturation and total hemoglobin estimates in the neonatal brain using the semi-infinite slab model for FD-NIRS data analysis," *Biomed. Opt. Express* **5**(12), 4300–4312 (2014).
29. L. Spinelli, L. Zucchelli, D. Contini, M. Caffini, J. Mehler, A. Fló, A. L. Ferry, L. Filippin, F. Macagno, L. Cattarossi, and A. Torricelli, "In vivo measure of neonate brain optical properties and hemodynamic parameters by time-domain near-infrared spectroscopy," *Neurophotonics* **4**(4), 041414 (2017).
30. S. Ijichi, T. Kusaka, K. Isobe, K. Okubo, K. Kawada, M. Namba, H. Okada, T. Nishida, T. Imai, and S. Itoh, "Developmental changes of optical properties in neonates determined by near-infrared time-resolved spectroscopy," *Pediatr. Res.* **58**(3), 568–573 (2005).
31. M. Giovannella, D. Contini, M. Pagliazzi, A. Pifferi, L. Spinelli, R. Erdmann, R. Donat, I. Rocchetti, M. Rehberger, N. König, R. H. Schmitt, A. Torricelli, T. Durduran, and U. M. Weigel, "BabyLux device: a diffuse optical system integrating diffuse correlation spectroscopy and time-resolved near-infrared spectroscopy for the neuromonitoring of the premature newborn brain," *Neurophotonics* **6**(2), 025007 (2019).
32. A. De Carli, B. Andresen, M. Giovannella, T. Durduran, D. Contini, L. Spinelli, U. M. Weigel, S. Passera, N. Pesenti, F. Mosca, A. Torricelli, M. Fumagalli, and G. Greisen, "Cerebral oxygenation and blood flow in term infants during postnatal transition: BabyLux project," *Arch. Dis. Child Fetal Neonatal. Ed.* **104**(6), F648–F653 (2019).
33. Q. Fang and D. R. Kaeli, "Accelerating mesh-based Monte Carlo method on modern CPU architectures," *Biomed. Opt. Express* **3**(12), 3223–3230 (2012).
34. S. Brigadoi, P. Aljabar, M. Kuklisova-Murgasova, S. R. Arridge, and R. J. Cooper, "A 4D neonatal head model for diffuse optical imaging of pre-term to term infants," *Neuroimage* **100**, 385–394 (2014).
35. F. Ohtsuki, "Developmental changes of the cranial bone thickness in the human fetal period," *Am. J. Phys. Anthropol.* **46**(1), 141–153 (1977).
36. J. Heiskala, T. Neuvonen, P. E. Grant, and I. Nissilä, "Significance of tissue anisotropy in optical tomography of the infant brain," *Appl. Opt.* **46**(10), 1633–1640 (2007).
37. J. Dobbing and J. Sands, "Quantitative growth and development of human brain," *Arch. Dis. Child.* **48**(10), 757–767 (1973).
38. D. A. Boas, J. P. Culver, J. J. Stott, and A. K. Dunn, "Three dimensional Monte Carlo code for photon migration through complex heterogeneous media including the adult human head," *Opt. Express* **10**(3), 159–170 (2002).
39. Y. Jauregui-Sánchez, P. Clemente, P. Latorre-Carmona, E. Tajahuerce, and J. Lancis, "Signal-to-noise ratio of single-pixel cameras based on photodiodes," *Appl. Opt.* **57**(7), B67–B73 (2018).
40. D. Contini, F. Martelli, and G. Zaccanti, "Photon migration through a turbid slab described by a model based on diffusion approximation I Theory," *Appl. Opt.* **36**(19), 4587–4599 (1997).
41. A. Sassaroli, F. Martelli, G. Zaccanti, and Y. Yamada, "Performance of fitting procedures in curved geometry for retrieval of the optical properties of tissue from time-resolved measurements," *Appl. Opt.* **40**(1), 185–197 (2001).
42. D. Comelli, A. Bassi, A. Pifferi, P. Taroni, A. Torricelli, R. Cubeddu, F. Martelli, and G. Zaccanti, "In vivo time-resolved reflectance spectroscopy of the human forehead," *Appl. Opt.* **46**(10), 1717–1725 (2007).